PNAS
www.pnas.org

Supplementary Information for

Ternary Nitride Semiconductors in the Rocksalt Crystal Structure

Sage R. Bauers[*1], Aaron Holder[1,2], Wenhao Sun[3,4], Celeste L. Melamed[1,5], Rachel Woods-Robinson[1,3,4], John Mangum[5], John Perkins[1], William Tumas[1], Brian Gorman[5], Adele Tamboli[1], Gerbrand Ceder[3,4], Stephan Lany[1], Andriy Zakutayev[*1]

Sage Bauers / Andriy Zakutayev
Email: sage.bauers@nrel.gov, andriy.zakutayev@nrel.gov

This PDF file includes:

Supplementary text
Figs. S1 to S3
Tables S1 to S4
References for SI reference citations

Other supplementary materials for this manuscript include the following:

Calculated crystallographic information files (CIFs) for $MgTiN_2$, $MgZrN_2$, $MgHfN_2$, and Mg_2NbN_3

www.pnas.org/cgi/doi/10.1073/pnas.1904926116

Supplementary Information Text

Materials and methods. $Mg_xTM_{1-x}N_y$ (*TM* = Ti, Zr, Nb, Hf) films were deposited on 50.8x50.8x1.1mm^3 glass substrates via radio frequency magnetron co-sputtering at 30-60 watts from metallic targets (Mg 99.98+%, all *TM* 99.9+%). Sputter deposition occurred in close proximity to a cryogenic sheath at a pressure of 5 mT under 6 sccm each of Ar and N_2 (99.999+%) gases in a vacuum chamber with base pressure < 10^{-7} torr (1). Nitrogen was introduced through an RF plasma source operating at 350W. Sputter targets were oriented obliquely to the stationary substrates such that a 1-D gradient in metal composition was created, with approximately 1% change in cation composition per mm (2). During growth, an orthogonal temperature gradient was passively induced by partial thermal contact of the glass substrate to a heated platen. The continuously varying processing conditions present on the sample surface were discretized into a 44-point grid. The specific points described in this study were selected for growth temperatures of 400°C and $Mg_{G-3+x}TM_{1-x}N_{G-2}$ compositions of x≈0 (stoichiometric) and x≈0.5 (Mg-rich). More information about the synthesis methods can be found in our previous publication (3).

X-ray diffraction data were collected with an approx. 1mm spot size at the Stanford Synchrotron Radiation Lightsource (SSRL) on beamline 1-5 at an energy of 15.5 keV on a CCD area detector. Rutherford backscattering (RBS) measurements were performed on a National Electrostatics Corporation 3S-MR10 instrument with a 2MeV alpha particle beam with 2mm spot size along the composition gradient, and analyzed using the RUMP package (4). Film thickness was determined by stylus profilometry using a Dektak 8 profilometer. Transmission electron microscopy (TEM) and energy dispersive x-ray spectroscopy (EDX) were performed using an FEI Talos F200X microscope operating at an accelerating voltage of 200 kV on a $MgHfN_2$ lamella prepared via ion beam milling and lift-out using an FEI Helios Nanolab dual beam SEM/FIB.

Transmission and reflection spectra were collected on a custom thin film optical spectroscopy system with spot size below 1mm^2 and absorption spectra were determined from these data together with film thickness. Transport measurements from Mg-rich compositions and epitaxial films were measured using a Lakeshore 8425 Hall probe equipped with a 2T superconducting magnet and variable temperature sample environment. Temperature-dependent resistivity measurements were made on combinatorial films cut into small chips of ca. 5x5 mm^2, and Hall measurements were made on separately prepared $MgZrN_2$ samples deposited on (100)- and (111)-oriented MgO substrates of the same size; in both cases small variation in composition is expected across these films. Experimental data used by this study have been analyzed using the COMBIgor software package (5) and are publicly available in the NREL high-throughput experimental materials database at https://htem.nrel.gov (6).

First principles density functional and many-body perturbation theory calculations were performed with the VASP code, employing the generalized gradient (GGA) and GW approximations, respectively (7, 8), with an on-site Coulomb interaction of U = 3eV for the *TM* cations. The ground state structure search was performed using the "kinetically limited minimization" approach, which is unconstrained and does not require prototypical structures from databases (9). Seed structures are generated from random lattice vectors and atomic positions, subject to geometric constraints to avoid extreme cell

shapes, and to observe minimal interatomic distances (2.8 Å for cation-cation and anion-anion pairs, 1.9 Å for cation-anion pairs). New trial structures are generated by the random displacement of one atom between 1.0 and 5.0 Å while maintaining the minimal distances. Trial structures are accepted if the total energy is lowered, and the number of trials equals the number of atoms in the unit cell. For each material, we sampled at least 100 seeds, using 16 atom cells for $AE_1TM_1N_2$ and 12 atom cells for Mg_2NbN_3. For the final ground state structures, a symmetry analysis was performed using the FINDSYM software (10), and a Crystallographic Information File (CIF) was generated (available in the supplementary information).

GW calculations were performed for these structures as described in Ref (11). Note that for compounds with the α-$NaFeO_2$ structure (SG 166) we find a slight distortion accompanied by an energy lowering of less than 1 meV/at, technically being described as a SG 13 structure with a larger 8 atom primitive cell and direct-forbidden electronic band gap. Disordered structures were generated through first-principles Monte-Carlo sampling in supercells between 64 and 96 atoms (5 random seeds per each case) using the Metropolis criterion for 2000 and 10000 K as effective temperature (12) for moderate and strong disorder, respectively. The motif decomposition shown in Fig. 3a was determined after equilibration at the respective T_{eff} by counting the cation coordination numbers for each N atom in the supercell. In order to calculate the electronic structure and optical absorption for these supercells, we used the single-shot-hybrid plus onsite potential (SSH+V) approach (11, 13), with parameters fitted to the GW calculations of the ground states (see Table S4). The density of states effective masses were determined as described in Ref (14).

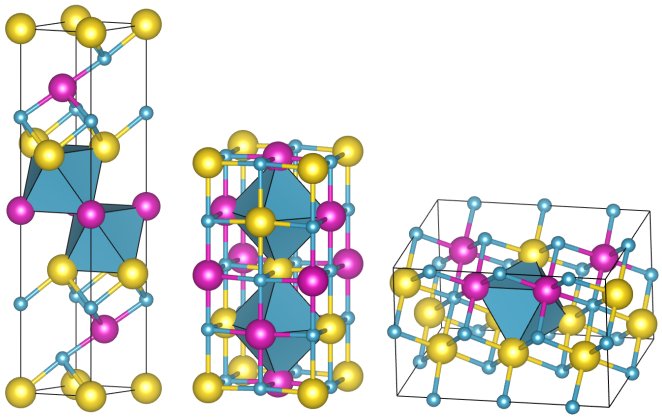

Fig. S1. Ordered rocksalt-derived structures of $Mg_{G-3}TMN_{G-2}$ (*TM*=Ti, Zr, Nb, Hf) ternary nitrides, with N shown in cyan, Mg in yellow, and *TM* in magenta. The nitrogen centered octahedra arrange as clustered motifs in S.G. 166 and S.G. 12 and as a dispersed motif in S.G. 141 (S.G.= Space Group. For motif descriptions, see main text).

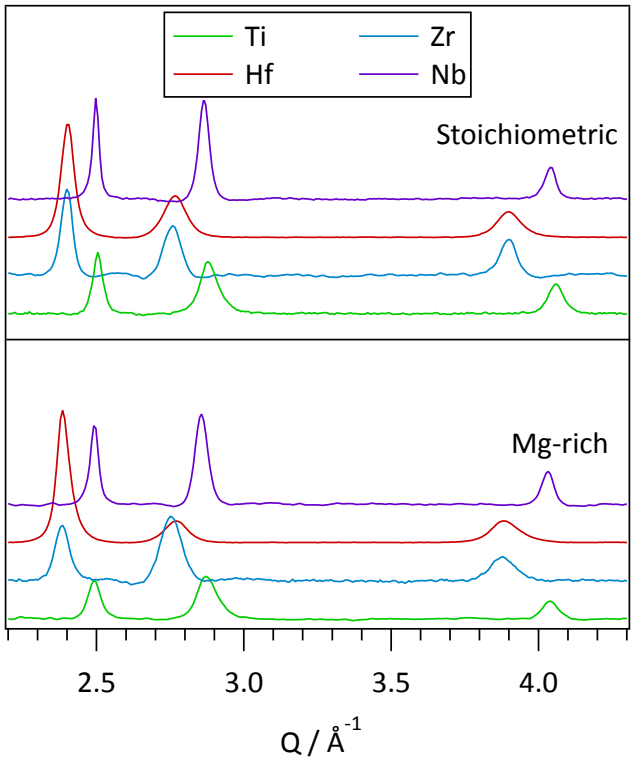

Fig. S2. Diffraction patterns from stoichiometric (top; x=0) and Mg-rich (bottom; x≈0.5) $Mg_{G-3+x}TM_{1-x}N_{G-2}$ thin films (G=4 for Ti, Zr, Hf and G=5 for Nb). The reflections for each pattern can be indexed to the NaCl (space group 225) structure.

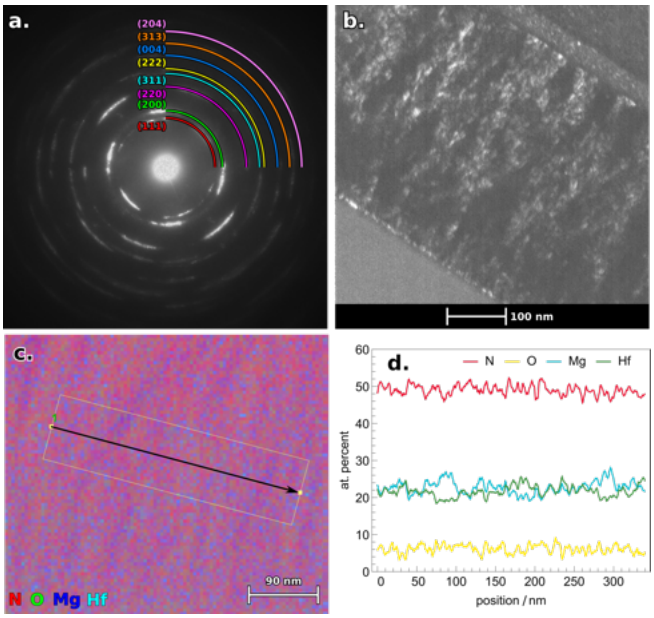

Fig. S3. TEM characterization of a $MgHfN_2$ lamella. **a.** SAED pattern exhibits reflections that are indexed to the NaCl structure. **b.** Dark field image highlights individual crystallites that are ~10nm in size. **c.** STEM-EDS map appears predominantly homogeneous, but with faint curtaining suggesting small fluctuations. **d.** Quantification of EDS map agrees with composition measured via Rutheford Backscattering and shows slight anti-correlated modulation in Mg and Hf compositions.

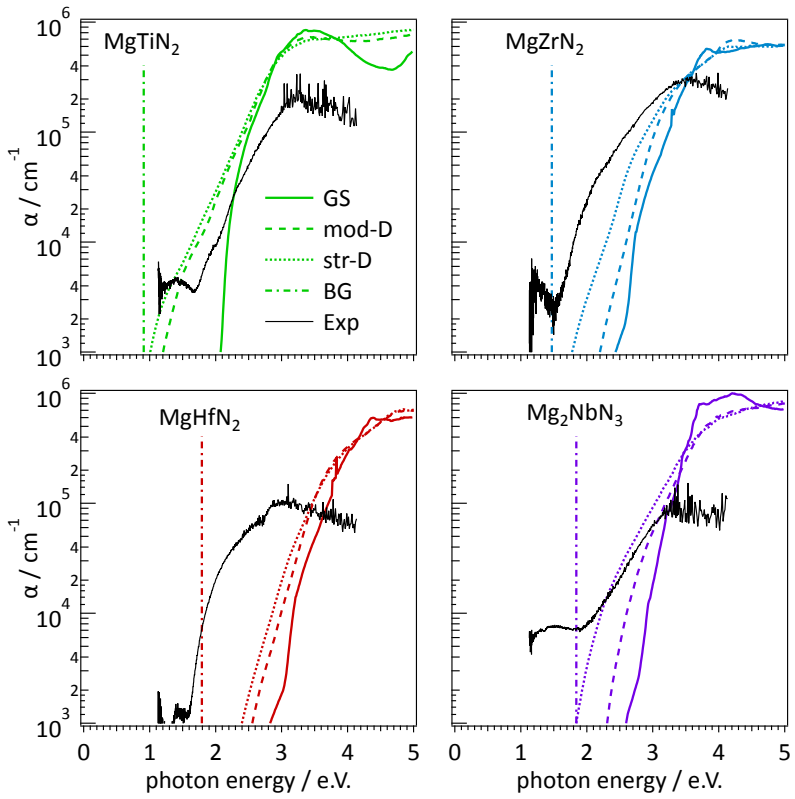

Fig. S4. Calculated absorption spectra for $Mg_{G\text{-}3}TMN_{G\text{-}2}$ with the rocksalt-derived ground state (GS) structure, and disordered structures with moderate- (mod-D) and strong- (str-D) disorder. The band gap of the ordered GS structure is shown by a vertical line. Overlayed are measured spectra for Mg-rich compositions (Exp).

Table S1. Calculated polymorph energies of the $Mg_{G-3}TMN_{G-2}$ ternary nitrides studied in this work (S.G.= Space Group).

Compound	S.G. 129 (eV/atom)	S.G. 141 (eV/atom)	S.G. 166 (eV/atom)	S.G. 15 (eV/atom)	S.G. 12 (eV/atom)
$MgTiN_2$	0.356	0.033	0.000		
$MgZrN_2$	0.470	0.000	0.016		
$MgHfN_2$	0.482	0.000	0.018		
Mg_2NbN_3				0.000	0.003
Mg_2TaN_3				0.017	0.000

Table S2. Lattice parameters, peak widths, and absorption onsets ($\alpha=10^4$ cm^{-1}) for experimental (Exp) $Mg_{G-3+x}TM_{1-x}N_{G-2}$ thin films (G=4 for Ti, Zr, Hf and G=5 for Nb). Absorption values are for Mg-rich compositions ($x\approx0.5$). Also displayed are calculated values for the predicted volume-based lattice parameters of the rocksalt-derived ground-state (GS) $Mg_{G-3}TMN_{G-2}$ structures, and the calculated absorption onsest ($\alpha=10^3$ cm^{-1}) of $Mg_{G-3}TMN_{G-2}$ in ground-state (GS, T_{eff} = 0 K), and with moderate- (mod-D, T_{eff} = 2000 K), and strong-disorder (str-D, T_{eff} = 10000 K).

Compound	(111) FWHM (Å^{-1})	Rocksalt lattice parameter (Å)		Energy at $\alpha=10^4$ cm^{-1} (Exp) or $\alpha=10^3$ cm^{-1} (calculated) (eV)			
	Exp	Exp	GS	Exp	GS	Mod-D	Str-D
$MgTiN_2$	0.042	4.26	4.33	2.0	2.1	1.2	1.0
$MgZrN_2$	0.065	4.54	4.57	1.8	2.5	2.2	1.8
$MgHfN_2$	0.053	4.52	4.53	1.9	2.9	2.6	2.0
Mg_2NbN_3 (rocksalt)	0.025	4.37	4.42	2.1	2.7	2.3	1.8

Table S3. Energy above ground state of disordered Mg-*TM*-N structures from Monte-Carlo simulations. Energies above the ground state for moderate (T_{eff} = 2000 K), strong (T_{eff} = 10000 K), and fully random (T_{eff} = ∞) disorder.

Compound	moderate (meV/at)	strong (meV/at)	random (meV/at)
$MgTiN_2$	18±4	30±6	52±8
$MgZrN_2$	16±3	22±8	32±7
$MgHfN_2$	20±3	28±9	45±11
Mg_2NbN_3 (hex)	24±7	53±14	123±34
Mg_2NbN_3 (rocksalt)	13±3	35±9	45±6

Table S4. Parameters for non-self-consistent SSH+*V* calculations. The values for the Fock exchange (α) and onsite potential (*V*) were fitted to GW calculations of the ordered ground states to reproduce the GW band structure within about 0.02 eV at E_g and about 0.1 eV at $2\times E_g$. The onsite-potential acts on the *TM-d* orbitals only. For Mg_2NbN_3, both the hexagonal lattice (hl) and rock-salt derived (rs) structures were used.

	$MgTiN_2$	$MgZrN_2$	$MgHfN_2$	Mg_2NbN_3-hl	Mg_2NbN_3-rs
α (%)	10.2	11.9	14.3	10.6	13.1
V (eV)	0.21	0.65	0.27	1.17	1.30

References

1. Bikowski A, et al. (2017) Design of Metastable Tin Titanium Nitride Semiconductor Alloys. *Chem Mater* 29(15):6511–6517.
2. Caskey CM, et al. (2015) Semiconducting properties of spinel tin nitride and other IV_3N_4 polymorphs. *J Mater Chem C* 3(6):1389–1396.
3. Bauers SR, et al. (2019) Composition, structure, and semiconducting properties of $Mg_xZr_{2-x}N_2$ thin films. *Jpn J Appl Phys* 58(SC):SC1015.
4. Doolittle LR (1986) A semiautomatic algorithm for rutherford backscattering analysis. *Nucl Instruments Methods Phys Res Sect B Beam Interact with Mater Atoms* 15(1–6):227–231.
5. Talley KR, et al. (2019) COMBIgor: data analysis package for combinatorial materials science. Available at: http://arxiv.org/abs/1904.07989.
6. Zakutayev A, et al. (2018) An open experimental database for exploring inorganic materials. *Sci Data* 5:180053.
7. Kresse G, Joubert D (1999) From ultrasoft pseudopotentials to the projector augmented-wave method. *Phys Rev B* 59(3):1758–1775.
8. Shishkin M, Kresse G (2006) Implementation and performance of the frequency-dependent G W method within the PAW framework. *Phys Rev B* 74(3):035101.
9. Arca E, et al. (2018) Redox-Mediated Stabilization in Zinc Molybdenum Nitrides. *J Am Chem Soc* 140(12):4293–4301.
10. Stokes HT, Hatch DM, IUCr (2005) *FINDSYM* : program for identifying the space-group symmetry of a crystal. *J Appl Crystallogr* 38(1):237–238.
11. Lany S (2013) Band-structure calculations for the 3 d transition metal oxides in G W. *Phys Rev B* 87(8):085112.
12. Ndione PF, et al. (2014) Control of the Electrical Properties in Spinel Oxides by Manipulating the Cation Disorder. *Adv Funct Mater* 24(5):610–618.
13. Lany S, et al. (2017) Monte Carlo simulations of disorder in ZnSn N 2 and the effects on the electronic structure. *Phys Rev Mater* 1(3):035401.
14. Lany S (2015) Semiconducting transition metal oxides. *J Phys Condens Matter* 27(28):283203.